NJC

PAPER

View Article Online
View Journal

Cite this: DOI: 10.1039/c8nj00378e

Microwave assisted poly(3,4-ethylene-dioxythiophene)–reduced graphene oxide nanocomposite supported Pt as durable electrocatalyst for polymer electrolyte fuel cells

S. Vinod Selvaganesh, *[ab] P. Dhanasekaran,[a] Raghuram Chetty [b] and Santoshkumar D. Bhat *[a]

Received 22nd January 2018,
Accepted 9th May 2018

DOI: 10.1039/c8nj00378e

rsc.li/njc

Mixed ionic-electronic conductors (MIECs) were explored for various applications due to their ionic and electronic species as separate charge carriers. MIECs have received considerable focus for polymer electrolyte fuel cell (PEFC) electrodes, electrocatalytic reactors, and gas separating membranes. Among MIECs, combinations of conducting polymers on highly conducting graphitic carbon nanostructures are particularly attractive because of their catalytic properties, electrochemical stability, and versatility for implementing various applications. In this regard, an optimum composition of a conducting polymer poly(3,4-ethylenedioxythiophene) (PEDOT) on reduced graphene oxide (rGO) supported platinum improved fuel cell performance and long-term durability. PEDOT was prepared by a micelle-mediated reverse-micro-emulsion technique, followed by grafting it over the GO. Further, Pt was deposited on PEDOT–GO using a microwave-assisted polyol method. The morphological and microstructural characteristics of electrocatalysts were investigated using different techniques. The optimum level of PEDOT embraced on rGO supported Pt retained 60% of initial ECSA and cell performance, even after 10 000 potential cycles between 1 and 1.5 V.

Introduction

The successful commercialization of polymer electrolyte fuel cells (PEFCs) depends on an efficient and stable electrode material, particularly the cathode. Generally, platinum on carbon (Pt/C) is widely used as a potential electrocatalyst for an oxygen reduction reaction (ORR) in PEFCs. However, corrosion of carbon followed by Pt degradation limits the usage of conventional carbon sources such as Vulcan XC72R and carbon black towards PEFC commercialization.[1,2] Hence, the present research is focused towards finding stable and active materials for Pt that can principally meet PEFC durability targets. Prerequisites for support materials such as high surface area, high electronic conductivity, and better corrosion stability under a PEFC operating environment, lead towards higher graphitic carbon nanostructures such as carbon nanotubes (CNTs), carbon nanofibers (CNFs), and graphene.[3–6]

Graphene among the aforesaid graphitic structures is particularly attractive owing to its high surface area, superior stiffness, strength, thermal and electrical conductivities, electronic transport properties, and chemical and thermal inertness.[7–9] In addition, graphene nanosheets and nanoribbons are known to offer a stable backbone structure for a composite electrocatalyst and a high-surface area that increases the contact between deposited metal catalysts and an electrolyte.[7] Graphene, as a constituent of the electrode material, overcomes many of the limitations of activated carbon.[10,11] The above mentioned properties render graphene superior to any other forms of activated carbon. However, there are certain drawbacks faced while anchoring Pt catalyst on graphene, which include poor dispersion of graphene sheets in various solvents prior to metal deposition. Besides, the conductivity of the graphene sheets is compromised/haggled in the process.[12,13] Hence, an alternative effective way to deposit Pt over graphene is highly essential. Technical difficulties involved in the dispersion of graphene in various solvents prior to fabrication of electrocatalysts have led to the preparation of graphene oxide (GO) which makes them soluble in most solvents. Further surface modification to GO offers an added advantage, ascribed to the presence of oxygen functional groups on its surface.

GO nanosheets contain carboxyl and hydroxyl functional groups on their surfaces and edges that are considered active

[a] CSIR-Central Electrochemical Research Institute-Madras Unit, CSIR Madras Complex, Chennai-600 113, India. E-mail: svsganesh.dr@gmail.com, sdbhat@cecri.res.in; Fax: +91-44-22542456; Tel: +91-44-22544564
[b] Department of Chemical Engineering, Indian Institute of Technology Madras, Chennai-600 036, India

sites; these can be used for chemical functionalization after which they are expected to exhibit electronic and high proton conductivity.[14–17] According to literature reports, GO nanosheets as support materials for Pt electrocatalyst are quite promising and show better ORR activity.[18,19] In this regard, embedding a mixed conducting polymer over GO is interesting due to the expected synergistic effect brought about by the ensuing composite. Conducting polymers such as polyaniline (PANI), polypyrrole (PPy), and poly(3,4-ethylenedioxythiophene) (PEDOT) show good electrochemical activity and stability and are promising candidates as hybrid electrodes for various electrochemical applications.[20,21] PEDOT is the most promising conducting polymer in view of its high electrical conductivity and is used as electrode material for a wide range of electrochemical applications.[22,23] Owing to synergistic physical properties such as electrochemical, mechanical, and electrical behaviour, a composite of PEDOT and GO could act as durable material to support Pt nanoparticles, which can enhance the performance of a Pt electrocatalyst.[24] In the present study, PEDOT embraced with a GO composite forms a new class of mixed ionic-electronic conductors (MIECs) that are explored towards fuel cell applications. Catalyst support that can incorporate high activity and durability through its interaction with Pt is likely to be very promising for PEFC applications.

In the present study, a hybrid MIEC-based composite support of PEDOT incorporated on reduced GO (rGO) for fuel cell operation was explored. PEDOT was prepared by a micelle mediated reverse-micro-emulsion technique followed by the formation of different compositions of MIEC by varying the ratio of PEDOT with respect to rGO. Pt nanoparticles were deposited on MIEC through a polyol method. Morphology, microstructural effects, and surface compositions of prepared electrocatalyst were evaluated using an X-ray diffraction method (XRD), Raman spectroscopy, field emission-scanning electron microscopy (FE-SEM), and transmission electron microscopy (TEM). Cyclic voltammetry and steady state fuel cell performance were carried out to assess the influence the prepared electrocatalyst in the overall performance. An accelerated stress test (AST) protocol towards transport application between 1 and 1.5 V was employed to analyse stability of the supports and Pt in an actual fuel cell environment under stringent operating conditions.

Experimental

Preparation of PEDOT, GO, and PEDOT–GO composites

PEDOT was synthesized by reverse cylindrical micelle-mediated interfacial polymerization using EDOT.[25] In brief, 4.75 g of sodium bis(2-ethylhexyl) sulfosuccinate (AOT) was dissolved in 70 mL of cyclohexane, which subsequently forms the reverse cylindrical micelles. Further, 0.36 mL of aqueous $FeCl_3$ solution was added drop-wise into the above mixture, which results in a yellow viscous solution. Then, 0.25 g of ethylenedioxythiophene (EDOT) was added, and the polymerization of EDOT was confirmed by a slow colour transition from yellow to violet. The polymerization of the EDOT monomer was performed at a temperature less than 20 °C. The resultant polymeric substance was washed with acetonitrile/methanol mixture in order to remove AOT and the residual reagents. GO was prepared from graphite flakes using Hummers' method.[26] PEDOT–GO composites were formed by dispersing the required composition of PEDOT and GO in ethanol with overnight stirring. Subsequently, the formed slurry was dried at 100 °C and gently ground together to form PEDOT embedded GO nanosheets. Various ratios of PEDOT : GO were synthesized *viz.*, 1 : 1, 2 : 1, 3 : 1, 4 : 1, and 5 : 1 and were labelled as PG1, PG2, PG3, PG4, and PG5, respectively.

Deposition of Pt nanoparticles on PEDOT, GO, and PEDOT–GO nanocomposite

Pt (30 wt%) deposited on PEDOT (Pt/PEDOT), rGO (Pt/rGO), and PEDOT–rGO(PG) nanocomposite was carried out by an ethylene glycol reduction method. In brief, the required amount of support material such as PEDOT, GO, or PEDOT–GO nanocomposite was dispersed in ethylene glycol–water (3 : 1) solution. To this dispersion, $H_2PtCl_6{\cdot}6H_2O$ (Aldrich) was added dropwise from a burette. Further, the pH of the solution was adjusted to 11–13 by NaOH addition and the mixture was refluxed at 140 °C for 6 h in a round bottom flask followed by microwave irradiation for 2 min with 30 s pulses. Finally, Pt-deposited PEDOT, rGO, and PG were separated from ethylene glycol solution after repeated washing with copious amount of distilled water followed by ethanol and drying in a hot air oven at 80 °C for 12 h. It is inferred that ethylene glycol itself acts as a reducing agent for the formation of uniform deposits of Pt on various supports Besides, oxidation products resulting from the ethylene glycol oxidation reaction could interact with Pt, thereby stabilizing the Pt nanoparticles.[27] The microwave irradiation also led to exfoliation of GO to form multiple layers of reduced graphene oxide (rGO), which is akin to other literature observations.[28,29]

Physical characterization

Powder X-ray diffraction (PXRD) studies were conducted with a BRUKER-binary V3 powder diffractometer using CuKα radiation (λ = 1.5406 Å) to analyse the change in crystallinity and crystallite size of Pt in Pt/PEDOT, Pt/rGO, and Pt/PG composite. Raman spectra were recorded on a Nanophoton Raman-11 spectrometer with a 532 nm line Nd-YAG laser. The surface morphologies, average particle size of Pt, and surface atomic compositions for various electrocatalyst were examined using a TESCAN MIRA 3 field emission-scanning electron microscope (FE-SEM) with energy dispersive X-ray spectrometry (EDX), transmission electron microscopy (TEM), and high resolution-transmission electron microscopy (HR-TEM) using a Tecnai G20 and G30, respectively. Inductively coupled plasma-optical emission spectroscopy (ICP-OES) analysis was carried out for the product water collected from the cathode exhaust to analyse for Pt that may have leached out along with product water during AST.

Fabrication and evaluation of membrane electrode assemblies (MEAs)

MEAs with an active area of 25 cm^2 were fabricated following a procedure reported in our earlier study.[30] To prepare a catalyst

layer, the required amount of the catalysts (Pt_{40}/C-Alfa Aesar for anode and Pt_{30}/PEDOT, Pt_{30}/rGO, or Pt_{30}/PG composite for cathode) was dispersed in water–isopropyl alcohol (IPA) solution followed by ultrasonication in a water bath. Further, 7 and 30 wt% of Nafion® (Dupont) ionomer was added to the anode and cathode slurry, respectively, with continuous sonication for 1 h. The resultant slurry was coated onto a commercial gas-diffusion layer (GDL-DC-35). Both anode and cathode had a platinum loading of 0.2 mg cm^{-2}, which was kept constant in all the MEAs. Subsequently, a thin layer of Nafion® dispersion (5 wt%) diluted with IPA in 1 : 1 ratio was brush-coated over the surface of each electrode to provide better interface contact between the catalyst layer and the polymer electrolyte. Finally, MEAs were obtained by hot pressing the cathode and anode on either side of a pre-treated Nafion-212 membrane at 60 kg cm^{-2} at 130 °C for 2 min. MEAs were evaluated using a conventional fuel cell fixture with a parallel serpentine flow field setup procured from M/s Fuel Cell Technologies Inc., US. Prior to measuring polarization data, the cells were equilibrated at constant potential for 6 h at 60 °C. The polarization data were recorded at varying load current-densities at 60 °C with the recommended stoichiometry of hydrogen (1.2) and oxygen (3) under ambient pressure on a Bio-Logic Science Instruments Corporation (FCT150S).

Accelerated stress test (AST)

AST was carried out following a detailed standard durability testing protocol.[31] In brief, AST was performed by potential cycling of the cathode in PEFC between 1 and 1.5 V with respect to the dynamic hydrogen electrode (DHE) using a Potentiostat (Autolab-PGSTAT 30) with the leads for reference and counter electrodes connected to the cell anode, and the lead for the working electrode connected to the cell cathode. The test was conducted at a cell temperature of 75 °C with humidified hydrogen at a flow rate of 1.2 stoichiometry at 1 A cm^{-2} and 100 mL min^{-1} of nitrogen to cathode, respectively. Cell polarization and cyclic voltammetry (CV) for measuring electrochemical surface area (ECSA) were conducted at frequent intervals of AST. A CV study was conducted to determine the hydrogen adsorption/desorption charge (H_{ad}/H_{des}) for PEFC cathodes using a potentiostat (Autolab-PGSTAT 30) with cell set-up and gas flow rates being the same as for AST. CVs were recorded between 0.05 and 1 V (*vs.* DHE) at a sweep rate of 50 mV s^{-1} at room temperature (~25 °C). CVs were repeated until stable and reproducible voltammograms were obtained. The region between 0.05 and 0.4 V, corresponding to the H_{ad}/H_{des} region, was used to measure the ECSA of the catalyst. ECSA of the Pt catalyst was estimated from the equation given below:

$$\mathrm{ECSA}\ \left(\mathrm{cm}^2\ \mathrm{g_{Pt}}^{-1}\right) = \frac{Q_{\mathrm{H}}\ \left(\mu\mathrm{C\ cm}^{-2}\right)}{210\ (\mu\mathrm{C\ cm}^{-2}) \times L\ (\mathrm{g_{Pt}\ cm}^{-2})}$$

where, Q_H represents the charge of hydrogen adsorption/desorption and is taken as 210 μC cm^{-2} for a monolayer of H_2 adsorbed/desorbed on smooth platinum surface, and L is the loading of platinum in g cm^{-2}.

Results and discussion

It is noteworthy that the microwave assisted polyol method provides simultaneous reduction of Pt and exfoliation of GO sheets resulting in the formation of reduced GO. The presumed schematic of microwave synthesis of PEDOT–rGO and Pt deposition is given in Scheme 1.

The surface morphology of the hybrid composite support was examined by FE-SEM. Fig. 1(a)–(f) shows the FE-SEM images for graphene oxide- and PEDOT-incorporated GO nanosheets. Fig. 1(a) reveals that GO sheets with multiple layers formed with an exfoliated structure derived from graphite. Fig. 1(c)–(f) reveals the various ratios of PEDOT embedded on GO nanosheets and it can be observed that PEDOT distribution varies as we go through various ratios of PEDOT to GO. Further, the Pt particle size and variation over distribution on PEDOT, rGO, and PG were analysed by TEM. Fig. 2(a)–(d) shows the TEM micrographs of Pt deposited on PEDOT, rGO, and PG composites. Fig. 2(a) shows the TEM micrographs for Pt/rGO, which clearly displays Pt deposited on multiple layers of exfoliated rGO nanosheets and Pt particle size is observed to be 4–5 nm with spherical morphology. Fig. 2(b) shows Pt deposited on PEDOT, wherein the Pt particle size is found to be slightly higher than that of Pt on rGO. Fig. 2(c) and (d) reveals the Pt particle size and distribution on PG2 and PG3. It is clear from the images that the distribution of Pt on PG is quite random with more uniformity in the case of PG3 as seen from Fig. 2(e) and (f).

In addition, scanning transmission electron microscopy (STEM) and mapping images of Pt deposited on PG3 is given in Fig. 3(a)–(h). Fig. 3(a) and (b) shows the HR-TEM micrographs of Pt/PG3 taken at two different magnifications, which clearly shows the Pt nanoparticles distributed homogenously throughout the support. Similarly, the STEM images and overall mapping for Pt/PG3 is shown in Fig. 3(c) and (d) followed by the individual mapping images for Pt/PG such as Pt, carbon, sulphur, and oxygen represented in Fig. 3(e)–(h). It is clear from the mapping images that the constituent elements are uniformly dispersed over the carbon which evidently shows PEDOT embraced over the rGO and smaller sized Pt uniformly distributed over the PG3.

Powder XRD patterns for Pt deposited on PEDOT, rGO, and various compositions of PEDOT–GO nanocomposite are given in Fig. 4. The peak at 26° corresponding to C(002) plane is seen

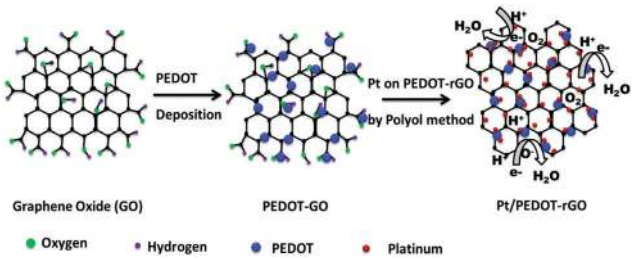

Scheme 1 Schematic representing the formation of PEDOT–GO and further simultaneous deposition of Pt and exfoliation of GO to rGO and possible ORR mechanism.

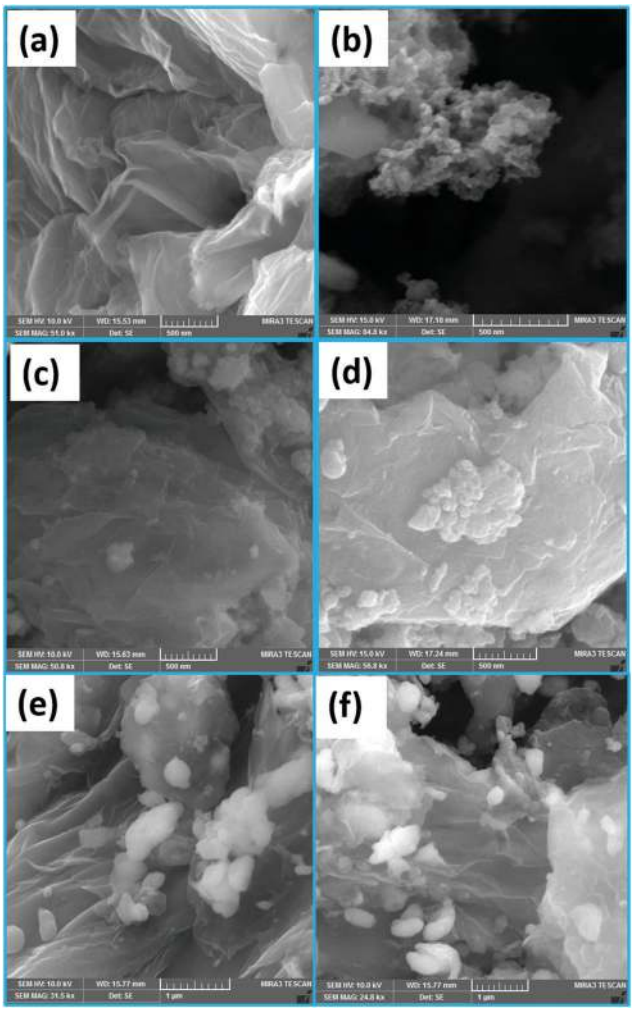

Fig. 1 FE-SEM micrographs of (a) rGO, (b) PEDOT, (c) PG1, (d) PG2, and (e and f) PG3.

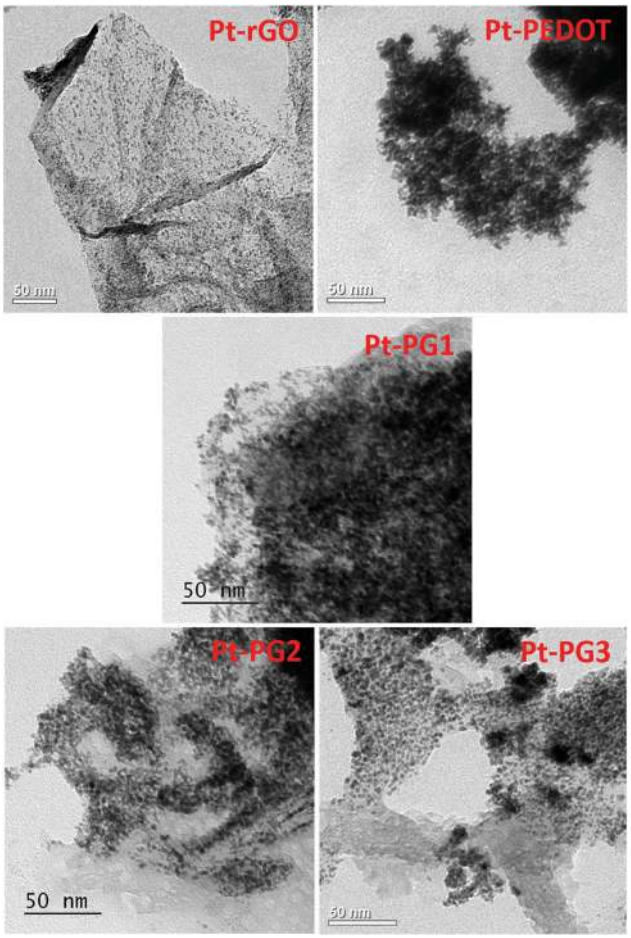

Fig. 2 TEM micrographs of Pt/rGO, Pt/PEDOT, Pt/PG1, 2, and 3.

in Pt/rGO and Pt/PG samples and is attributed to the graphitic nature of carbon and overlapping with the peak corresponding to PEDOT. Pt deposited on PEDOT, Pt/rGO, and Pt/PG electrocatalysts shows broad peaks at 39.9, 46.4, and 67.6° corresponding to (111), (200), and (220) lattice planes, confirming the face-centered cubic (fcc) structure of Pt metal particles (JCPDS no. 87-0647). The platinum crystallite size was calculated from full-width-at-half-maximum (FWHM) value for the (111) peak using the Scherrer equation.[32] The average Pt crystallite sizes in Pt/PEDOT, Pt/rGO, and Pt/PG electrocatalysts are furnished in Table 1 where it is observed that the Pt crystallite size varies constantly for Pt/PEDOT, Pt/rGO, and Pt/PG. The Pt crystallite size for Pt/rGO is slightly higher whereas for Pt/PEDOT and Pt/PG the sizes are comparable, which clearly shows the role of PEDOT in Pt dispersion.

Fig. 5 shows the Raman bands between 100–1100 cm^{-1} for PEDOT, GO, and PG. The sharp peaks observed for PEDOT at 980 and 570 cm^{-1} correspond to the oxyethylene ring deformation during polymerization of the EDOT monomer. In addition, the broad hump observed at 702 cm^{-1} is attributed to the deformation of the C–S–C bond during polymerization as seen in Fig. 5(a). The above peaks are shifted towards a higher wavenumber for the PG system as seen from Fig. 5(c) and (d) which could be attributed to π–π interactions between the PEDOT and graphitic carbon. This is also confirmed from literature reports that the π–π interactions between the PEDOT and graphitic carbon are established which could lead to surface functionalization of GO by PEDOT.

Fig. 6 shows the Raman spectra from 1100 to 3000 cm^{-1}. In the Raman spectra for GO and PEDOT–GO the distinctive peaks at 1300 and 1500 cm^{-1} correspond to the characteristic disordered structure of carbon and highly ordered graphitic carbon of sp^2 hybridized carbon. It was observed from the Raman spectra that with an increase in PEDOT content, the ratio of I_G/I_D corresponding to the graphitic and disordered peaks was slightly reduced with a simultaneous increase in the peak intensity corresponding to oxyethylene ring deformation. This could be attributed to the fact that with an increase in PEDOT on the surface, the graphitic nature is decreased due to surface functionalization. This is also confirmed from the literature reports that the π–π interactions between the PEDOT and graphitic carbon is established which could lead to the surface functionalization of GO by PEDOT.[33]

The performance data for PEFCs with Pt/PEDOT, Pt/rGO, and Pt/PG employed as cathode catalysts is presented in Fig. 7(a).

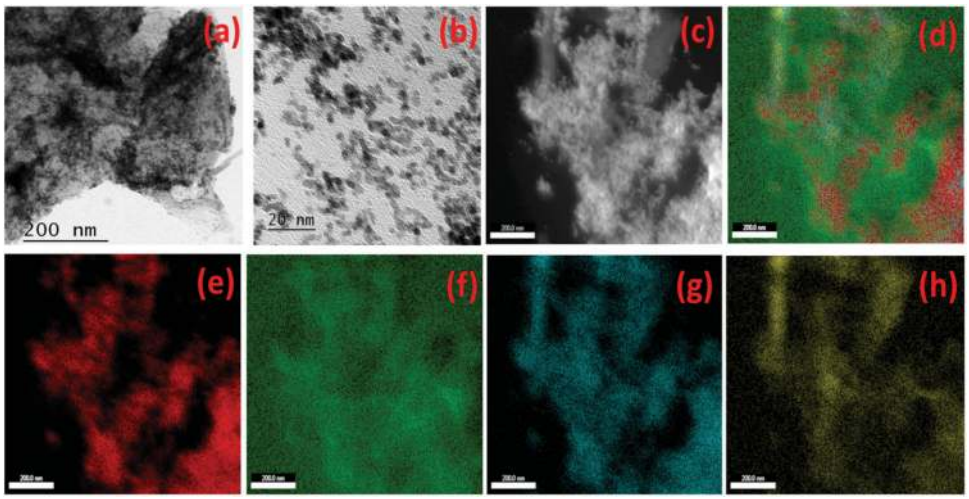

Fig. 3 HR-TEM, STEM and elemental mapping micrographs of Pt/PG3. (a and b) HR-TEM micrographs for Pt/PG3 at lower and higher magnification; (c and d) STEM and overall mapping images of Pt/PG3; (e–h) individual elemental images of Pt/PG3, (e) Pt, (f) carbon, (g) sulphur, and (h) oxygen.

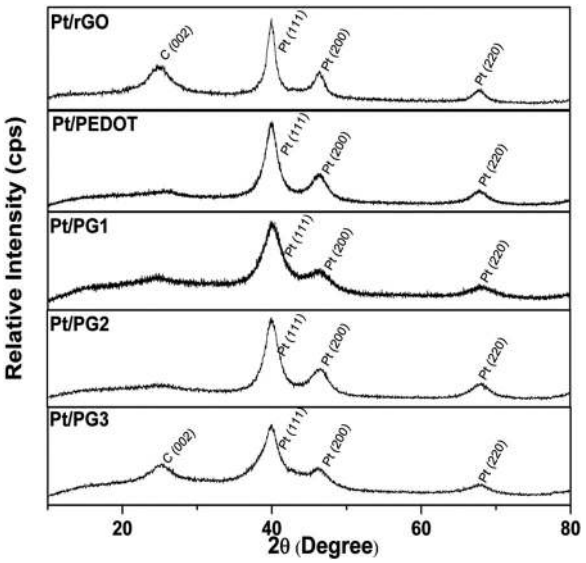

Fig. 4 Powder XRD pattern for Pt/PEDOT, Pt/rGO, and various nanocomposite supported Pt (Pt/PGs).

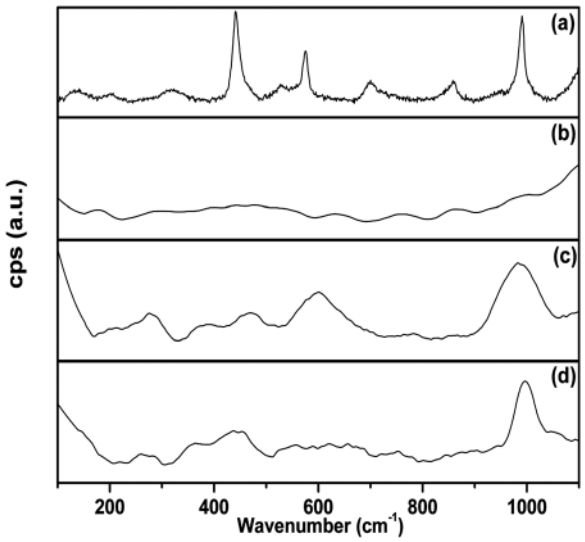

Fig. 5 Raman spectra from 100–1100 cm^{-1} for (a) PEDOT, (b) rGO, (c) PG2, and (d) PG3 nanocomposites.

Table 1 Pt crystallite size calculated from XRD and ECSA measured from CV before and after AST

Catalyst	Pt crystallite size (nm) from XRD	Pt ECSA from CV (m^2 g^{-1})	
		Before AST	After AST
Pt/PEDOT	4.8	34.69	23.47
Pt/rGO	6.5	22.81	19.31
Pt/PG1	3.9	32.63	—
Pt/PG2	4.2	38.43	—
Pt/PG3	3.4	41.32	31.28

From the polarization curves, it is clear that Pt/PG3 and Pt/PG4 electrocatalysts exhibited higher cell performance than Pt/PEDOT, Pt/PG1, Pt/PG2, Pt/PG5, and Pt/rGO in the entire polarization region. Among the Pt/PG composites, Pt/PG3 delivered the highest performance and Pt/PG4 was quiet comparable to that of Pt/PG3. However, upon further increasing the PEDOT ratio, the fuel cell performance was reduced, which could be due to higher amount of PEDOT embracing over rGO and obstructing the pathway of electron transfer. The increased performance for Pt deposited on optimum composition of PEDOT–rGO composites is attributed to the role played by the PEDOT as an additional charge carrier, which also helps in distribution of Pt on the surface of rGO. In addition, it was also observed that the PEFC comprising Pt/PEDOT also performs better which again shows the role of PEDOT as a desired support with increased electronic conductivity.

It is to be noted that along with PEDOT, rGO is also known to act as a charge-carrier and transport medium. The increased surface area of rGO leads to a higher charge transfer rate between the catalyst and the reactant intermediates. Moreover, in the

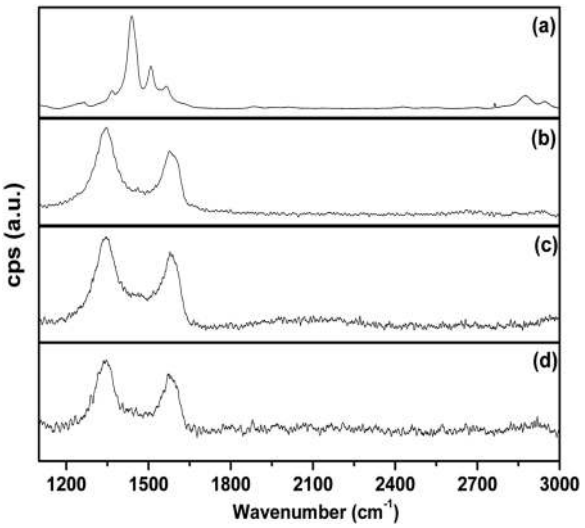

Fig. 6 Raman spectra from 1100–3000 cm^{-1} for (a) PEDOT, (b) rGO, (c) PG2, and (d) PG3.

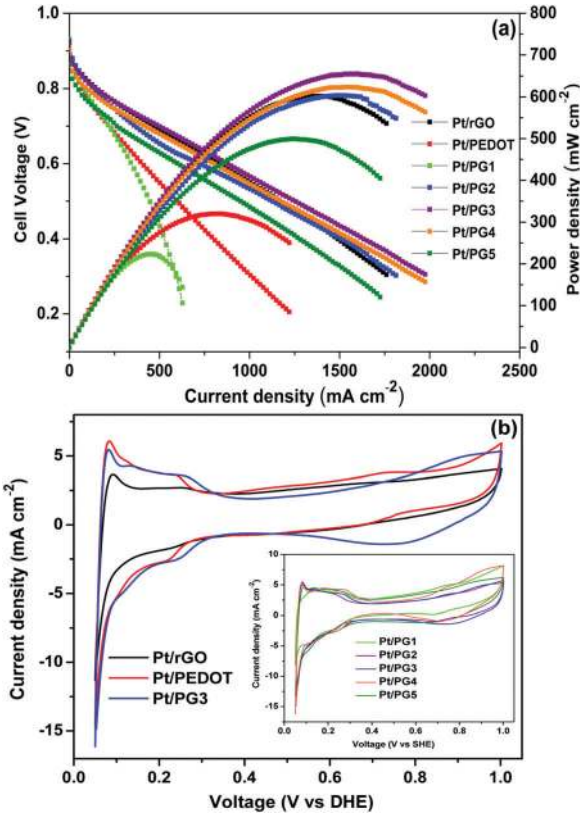

Fig. 7 Comparative (a) steady-state polarization and (b) CV curves recorded for Pt/rGO, Pt/PEDOT, and Pt/PG3 ((b-inset) CV curves for various Pt/PG nanocomposites).

case of the PG3 nanocomposite, the rGO backbone in the support structure is expected to increase the charge transport and thereby lower the Ohmic losses.[34]

Electrochemical surface area (ECSA) and electrochemical behaviour were observed by CV studies for PEFCs comprised of Pt/PEDOT, Pt/rGO, and Pt/PG3 as cathode catalysts, and the voltammograms are shown in Fig. 7(b-inset) showing various Pt/PG nanocomposites. From the CV, the hydrogen adsorption/desorption (H_{ad}/H_{de}) region at the potential range of 0.05 to 0.4 V (*vs.* DHE) was observed for all catalysts. The parallel region between 0.4 and 0.65 V corresponds to the double layer region and the hump at potentials >0.65 V is attributed to oxide formation/reduction of Pt. The H_{ad}/H_{de} charge for Pt/PG3 is highest followed by Pt/PEDOT, Pt/PG2, Pt/PG1, and Pt/rGO. From the CV, it is clear that ECSA for Pt deposited on Pt/PG3 and Pt/PG2 is higher in comparison to Pt/PG1. This is in good agreement with Pt distribution observed in TEM micrographs. The ECSA values estimated from the CV for the PEFC cathodes comprising Pt/PEDOT, Pt/rGO, Pt/PG1, Pt/PG2, Pt/PG3, Pt/PG4, and Pt/PG5 are 34.69, 22.81, 32.63, 38.43, 41.32, 40.26, and 33.74 $m^2\ g^{-1}$, respectively. The increased ECSA in the case of Pt on PG3, PG4, and PEDOT based supports over that from rGO is due to the availability of more anchoring sites. It is surmised that the sulphur groups on a surface act as anchoring sites for Pt thus leading to more homogeneous distribution of Pt on PEDOT and PG surfaces.

Following evaluation of the initial performance and measurement of ECSA values, Pt deposited on PEDOT, reduced graphene oxide, and a better performing catalyst among PG supported Pt (Pt/PG3) were chosen and subjected to durability studies. Precisely, the PEFCs comprised of Pt/PEDOT, Pt/rGO, and Pt/PG3 cathodes were assessed for stability by potential cycling between 1 and 1.5 V at 75 °C as discussed in the experimental part. During the potential transients, the cathode exhaust was connected to a CO_2 sensor. During potential cycling at higher potentials, there was a predictable performance loss due to independent processes such as oxidation of the support and subsequently Pt nanoparticles being leached out or agglomerated.[35]

During the AST, CO_2 emission of 90–110 ppm was initially observed for PEFCs with the Pt/PEDOT cathode, whereas for Pt/PG3 only 60–80 ppm was observed for the initial few cycles after which there was no CO_2 evolution. In the case of Pt/rGO up to 1000 cycles, initially 10–30 ppm of CO_2 emission was observed. The increased oxidation behaviour in the case of PEDOT shows vulnerability of this conducting polymer in this potential range.

Cyclic voltammetry and cell polarization studies were conducted at regular intervals of AST for Pt/PEDOT, Pt/rGO, and Pt/PG3 in order to correlate the loss in catalyst ECSA with performance loss. Performance data for PEFCs employing Pt/PEDOT, Pt/rGO, and Pt/PG3 as cathode electrocatalysts before and after AST are shown in Fig. 8. It was observed that PEFC with Pt/PEDOT showed a peak power performance of 605 mW cm^{-2} and after 6000 potential cycles of AST, it reduced to 476 mW cm^{-2}. Subsequently, upon continuing the AST up to 10 000 potential cycles, it reduced radically to 363 mW cm^{-2}. Whereas in the case of Pt/rGO, the initial performance was observed to be 320 mW cm^{-2} and after AST it was observed to be 270 and 250 mW cm^{-2} for 6000 and 10 000 potential cycles intervals, respectively. A similar trend in performance loss was observed for PEFC with Pt/PG3 which delivered a peak power

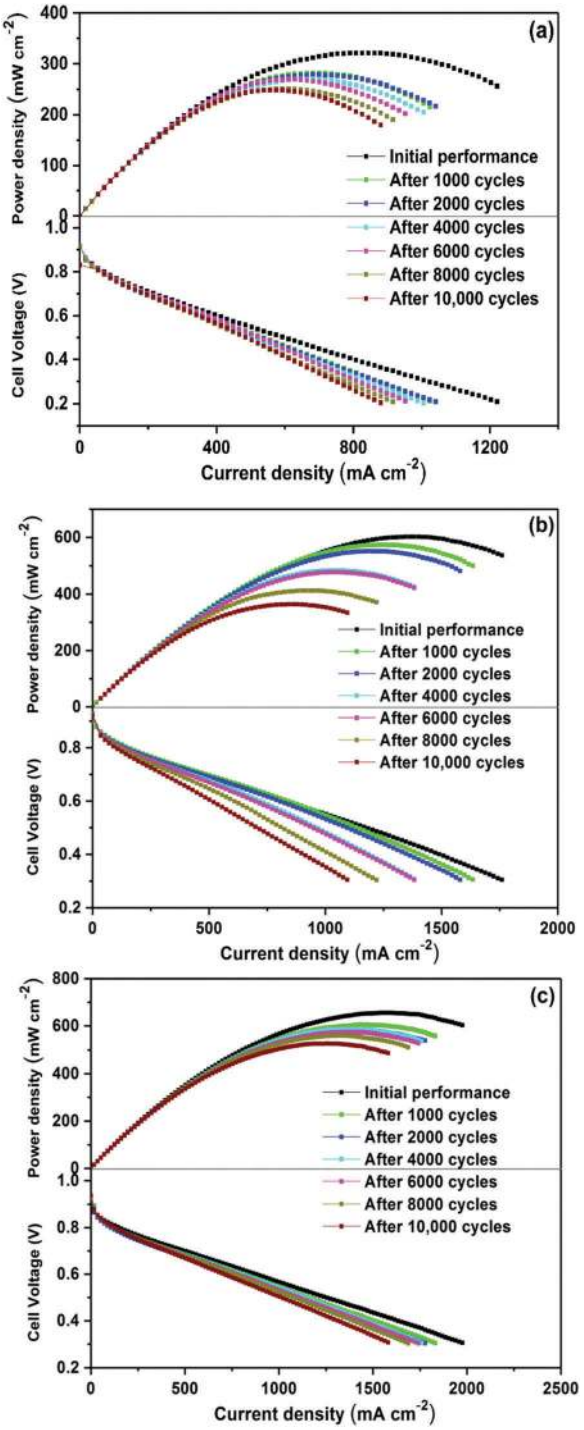

Fig. 8 Steady-state polarization curves at specific intervals of AST for (a) Pt/rGO, (b) Pt/PEDOT, and (c) Pt/PG3.

density of 655 mW cm^{-2} prior to subjecting the cell to AST and after AST it delivered a cell performance of 575 and 530 mW cm^{-2} for 6000 and 10 000 cycles of AST, respectively. The decline in cell performance in the case of Pt/PEDOT is comparable to that of Pt/rGO and Pt/PG3. Similarly, the deterioration in performance for PEFC with the Pt/PEDOT cathode was 40% after 10 000 potential cycles in relation to 22 and 19% for Pt/rGO and Pt/PG3 measured from the loss in peak power performance. It was observed that the drop in current density for Pt/PEDOT was more at all three measured voltages.

The minimal loss in performance after 10 000 potential cycles of AST for Pt/PG3 as the cathode catalyst suggests that it is corrosion resistant during fuel-cell operation, possibly due to a synergetic interaction of PEDOT–rGO with the Pt electrocatalyst. Indeed, rGO in the nanocomposite structure offers corrosion resistance and the sulphur groups on the surface act as anchoring sites for Pt leading to more homogeneous distribution of Pt on the PG surface. Moreover, the strong interaction between the rGO matrix and the sulphur groups in the PEDOT could also impart stability and corrosion resistance to the PG composite.[36]

In order to comprehend the loss in cell performance and ECSA for PEFCs with Pt/PEDOT, Pt/rGO, and Pt/PG3 cathodes, the loss in the steady-state performance and ECSA values during AST are presented in Fig. 9(a) and (b), respectively. It was observed that for PEFC comprising Pt/PEDOT as a cathode electrocatalyst, the cell performance and ECSA values though initially stable up to 4000 potential cycles, fell sharply

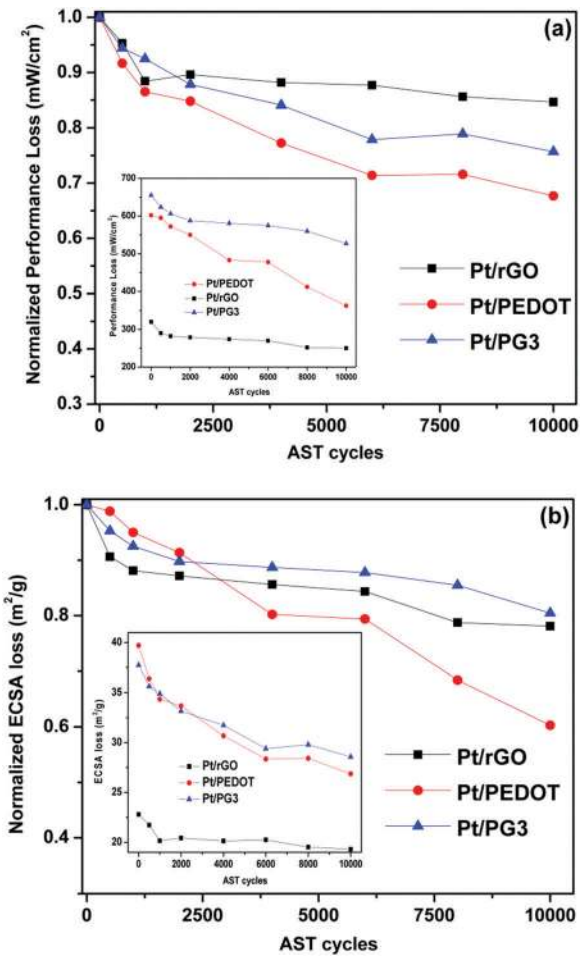

Fig. 9 Comparative plot depicting change in (a) steady-state performance loss, (b) normalized ECSA during AST for Pt/PEDOT, Pt/rGO, and Pt/PG3 electrocatalysts (inset showing absolute loss in performance and ESA during AST).

during AST. Whereas, for PEFC comprising Pt/rGO as a cathode electrocatalyst, the cell performance and ECSA values were comparatively stable up to 10 000 AST cycles with minimal loss. However, in the case of Pt/rGO, though the initial performance was low, the stability and resistance to oxidation was higher than the other two catalysts. This explains the role of rGO nanosheets in enhancing the durability of the catalyst as a whole. The graphene structure in Pt supported on PG electrocatalyst is known to create a conducting network, resulting in increased macroscopic electronic conductivity.[34,36] In addition, the conductive rGO network also facilitates electron transfer between the Pt-deposited PEDOT grains and the backing layer.[34]

The partial loss in ECSA and performance in the case of Pt/rGO may be due to preferential oxidation of PEDOT exposed in some regions of the catalyst layer and followed by loss of Pt active sites. The loss in ECSA for Pt/PEDOT was found to be 38% in relation to only 16 and 24% for Pt/rGO, Pt/PG3 cathode electrocatalysts, respectively. The initial and final ECSA values of the electrocatalysts after 10 000 potential cycles are furnished in Table 1. Likewise, the drop in performance for PEFCs with Pt/PEDOT, Pt/rGO, and Pt/PG3 as cathode catalysts after AST is 38, 21, and 19%, respectively after 10 000 cycles of AST as measured from the current density at 0.6 V. Hence, the change in steady-state polarization data are akin to the loss in ECSA values during AST. In addition, ICP-OES analysis was carried out for the product water collected from the cathode exhaust for possible Pt content. Indeed, during voltage transients particularly at cathode, there is a probability of Pt electrocatalyst dissolution in product water owing to support oxidation. In this study, the concentration of dissolute Pt for PEFCs with Pt/PEDOT, Pt/rGO, and Pt/PG3 cathodes are found to be 2.244, 0.629, and 0.778 mg L^{-1}, respectively.

These data corroborate with corrosion behaviour during AST suggesting that the PEDOT–rGO-based supports and nanocomposites are resistant to oxidation even under highly oxidizing conditions. The role of PEDOT in enhancing the catalytic activity and stability of the Pt/PG nanocomposite is based on the π–π interaction between the conducting polymer and the graphitic carbon[32] and the resulting charge transfer effect that leads to ameliorated catalytic activity of Pt nanoparticles. It is noteworthy that the unique electronic structure of rGO also helps in enhancing catalytic activity of the supported metal. In addition, the graphitic nature of the graphene nanosheets provides mechanical integrity and stability for the highly dispersed metal nanoparticles, resulting in increased stability of Pt/rGO and Pt/PG3. Thus, results confirm that the optimum composition of PEDOT–rGO with Pt (Pt/PG3) enhanced cell performance and long-term durability in PEFCs.

Conclusions

A stable support comprised of PEDOT embedded on reduced graphene oxide nanosheets to form PG composites for fuel cell operation was demonstrated. A microwave assisted polyol method provided simultaneous reduction of Pt and exfoliation of GO sheets resulting in formation of reduced GO. PEFC comprising a PEDOT–rGO nanocomposite-supported Pt cathode exhibited higher cell performance and durability. The deterioration in performance for PEFC with Pt/PEDOT cathode was 40% after 10 000 potential cycles in relation to 22 and 19% for Pt/rGO, Pt/PG3 electrocatalyst. The superior stability of the prepared composite is based on the synergistic role played by the PEDOT and graphene oxide. Besides, the strong Pt–PEDOT–rGO (Pt/PG3) interaction is known to play a critical role in the overall stability and retained initial fuel cell performance. Thus, an alternative stable support comprised of PEDOT and rGO for Pt could possibly overcome issues related to durability of the catalyst and carbon oxidation even during stringent PEFC operation conditions.

Conflicts of interest

All authors have approved the manuscript and agree with submission to New Journal of Chemistry. We have read and abided by the statement of ethical standards of this journal. The manuscript is submitted solely to this journal. The manuscript is not published or submitted elsewhere. The authors have no conflicts of interest to declare.

Acknowledgements

Dr S. D. Bhat thanks CSIR grant under CSIR-Young Scientist Award (DU-MLP-0090) Scheme. Dr S. Vinod Selvaganesh gratefully acknowledges DST-SERB for the National Post-Doctoral Fellowship (PDF/2016/002945) and Mr P. Dhanasekaran thanks CSIR for Research Associateship. We also thank Mr A. Rathishkumar, Senior Technical Officer, CSIR-CECRI for his help in TEM characterization.

References

1 K. H. Kangasniemi, D. A. Condit and T. D. Jarvi, *J. Electrochem. Soc.*, 2004, **151**, E125–E132.
2 P. J. Ferreira, Y. S. Horn, D. Morgan, R. Makharia, S. Kocha and H. A. Gasteiger, *J. Electrochem. Soc.*, 2005, **152**, 2256–2271.
3 X. Wang, W. Li, Z. Chen, M. Waje and Y. Yan, *J. Power Sources*, 2006, **158**, 154–159.
4 K. H. Kim, H. S. Oh and H. Kim, *Electrochem. Commun.*, 2009, **11**, 1131–1134.
5 S. Iijima, *Science*, 1991, **354**, 56–58.
6 R. Chetty, W. Xia, S. Kundu, M. Bron, T. Reinecke, W. Schuhmann and M. Muhler, *Langmuir*, 2009, **25**, 3853–3860.
7 M. S. Halper and J. C. Ellenbogen, *Supercapacitors: a brief overview*, Mitre Corporation, Virginia, 2006.
8 Y. Liu, H. Wang, J. Zhou, L. Bian, E. Zhu and J. Hai, *Electrochim. Acta*, 2013, **112**, 44–52.
9 I. Cha, E. J. Lee, H. S. Park, J. H. Kim, Y. H. Kim and C. Song, *Synth. Met.*, 2014, **195**, 162–166.
10 Y. Li, L. Tang and J. Li, *Electrochem. Commun.*, 2009, **11**, 846–849.

11 D. Chen, L. H. Tang and J. H. Li, *Chem. Soc. Rev.*, 2010, **39**, 3157–3180.
12 Y. L. Hsin, K. C. Hwang and Y. C. Tih, *J. Am. Chem. Soc.*, 2007, **129**, 9999–10010.
13 S. G. Peera, K. K. Tintula, A. K. Sahu, S. Shanmugam, P. Sridhar and S. Pitchumani, *Electrochim. Acta*, 2013, **108**, 95–108.
14 K. Zhang, X. Duan, X. Zhu, D. Hu, J. Xu and L. Lu, *Synth. Met.*, 2014, **195**, 36–43.
15 G. Compagnini, P. Russo, F. Tomarchio, O. Puglisi, L. D'Urso and S. Scalese, *Nanotechnology*, 2012, **23**, 505–601.
16 Y. Lu, Y. Jiang, W. Wei, H. Wu, M. Liu and L. Niu, *J. Mater. Chem.*, 2012, **22**, 2929–2934.
17 W. Si, W. Lei, Z. Han, Y. Zhang, Q. Hao and M. Xia, *Sens. Actuators, B*, 2014, **193**, 823–829.
18 L. Gan, H. Du, B. Lia and F. Kang, *Chem. Commun.*, 2011, **47**, 3900–3902.
19 J. N. Wang, Y. Z. Zhao and J. J. Niu, *J. Mater. Chem.*, 2007, **17**, 2251–2256.
20 H. S. White, G. P. Kittlesen and M. S. Wrighton, *J. Am. Chem. Soc.*, 1984, **106**, 5375–5377.
21 D. A. Mengistie, C. H. Chen, K. M. Boopathi, F. W. Pranoto, L. J. Li and C. W. Chu, *ACS Appl. Mater. Interfaces*, 2015, **7**, 94–100.
22 W. Li, J. Chen, J. Zhao, J. Zhang and J. Zhu, *Mater. Lett.*, 2005, **59**, 800–803.
23 F. Alvi, M. K. Ram, P. A. Basnayaka, E. Stefanakos, Y. Goswami and A. Kumar, *Electrochim. Acta*, 2011, **56**, 9406–9412.
24 C. Y. Chu, J. T. Tsai and C. L. Sun, *Int. J. Hydrogen Energy*, 2012, **37**, 13880–13886.
25 S. Vinod Selvaganesh, J. Mathiyarasu, K. L. N. Phani and V. Yegnaraman, *Nanoscale Res. Lett.*, 2007, **2**, 546–549.
26 W. S. Hummers and R. E. Offeman, *J. Am. Chem. Soc.*, 1958, **80**, 1339.
27 C. Bock, C. Paquet, M. Couillard, G. A. Botton and B. R. MacDougall, *J. Am. Chem. Soc.*, 2004, **126**, 8028–8037.
28 A. H. A. Monteverde Videla, S. Ban, S. Specchia, L. Zhang and J. Zhang, *Carbon*, 2014, **76**, 386–400.
29 J. Jeng, J. Amici, A. H. A. Monteverde Videla, C. Francia and S. Bodoardo, *J. Solid State Electrochem.*, 2017, **21**, 503–514.
30 P. Dhanasekaran, S. Vinod Selvaganesh and S. D. Bhat, *New J. Chem.*, 2017, **41**, 13012–13026.
31 Fuel Cell Technical Team Roadmap, US Department of Energy (USDoE), 2013.
32 S. Vinod Selvaganesh, G. Selvarani, P. Sridhar, S. Pitchumani and A. K. Shukla, *J. Electrochem. Soc.*, 2010, **157**, B1000–B1007.
33 Y. D. Quan, R. J. Francois and E. Sacher, *J. Phys. Chem. B*, 2005, **109**, 4481–4484.
34 K. Xu, G. Chen and D. Qiu, *J. Mater. Chem. A*, 2013, **1**, 12395–12399.
35 K. Kinoshita, J. T. Lundquis and P. Stonehart, *Electrochemistry*, 1973, **48**, 157–166.
36 H. Li, M. Sun, T. Zhang, Y. Fang and G. Wang, *J. Mater. Chem. A*, 2014, **2**, 18345–18352.